

Fig. 2. The viewpoints of a reflective surface with constant elevational gain lie on a caustic surface (red curve) defined in (4). All principal rays are tangent to the caustic.

would have with a true spherical sensor.¹ This property is not a feature of other shapes, e.g. hyperboloidal reflective surfaces, where the angular resolution increases with radial distance from the image centre.

B. Non-single viewpoint of constant elevational gain surfaces

The viewpoint of a constant-gain surface is not fixed: it varies with the elevational angle of view, as shown in Fig. 2. As derived in [4] using an approach described in [5], the locus of these viewpoints describe a so-called “caustic surface” whose profile is given by

$$\mathbf{x}_c(\theta) = \mathbf{x}_m(\theta) - \frac{1}{\alpha} r(\theta) \begin{pmatrix} \sin(\alpha\theta + \beta) \\ -\cos(\alpha\theta + \beta) \end{pmatrix}. \quad (4)$$

Apart from the trivial case of a planar reflective surface that is obtained from (3) by using the parameter values $\alpha = 1$, $\beta = 0$, i.e. $r(\theta) = r_0/\cos\theta$ resulting in $\mathbf{x}_c = (0, 2r_0)^\top$, surfaces with constant elevational gain do not have a fixed viewpoint (Fig. 2). Such surfaces can be regarded as a fixed viewpoint system as long as objects are far away compared to the size of the caustic surface, and resolution is low. However, for close objects this assumption is not valid, complicating the calibration of such catadioptric systems and limiting their applicability because algorithms in computer vision often assume a single viewpoint system. Baker and Nayar [2, 6] describe a family of catadioptric imaging systems that have a

¹The perspective mapping of the camera lens will introduce small deviations from the ideal constant angular resolution per pixel for large camera angles. For a camera lens with perfect perspective mapping, elevation angle ε and distance from image centre ϱ are related by $\varrho = f \tan \theta \stackrel{(2)}{=} f \tan[\frac{1}{\alpha}(\varepsilon - \beta + \frac{\pi}{2})]$, where f is the focal length of the camera lens in pixel. For $\theta = \frac{1}{\alpha}(\varepsilon - \beta + \frac{\pi}{2}) \ll 1$ the linear approximation $\varrho \approx f\theta = \frac{f}{\alpha}(\varepsilon - \beta + \frac{\pi}{2})$ is valid.

single, fixed viewpoint. However, as already mentioned, they do not offer a constant angular mapping.

In this paper we present a combination of reflective and refractive surfaces that has both desirable properties (constant elevational gain and single viewpoint). Recently, it has been shown that also a combination of two mirrors can be used to achieve various different “constant resolution” mappings while keeping a single viewpoint [7, 8]. As we will describe in the following sections, the use of a refractive surface allows to construct a very compact and rugged imaging system. This system builds on previous work [9] where a reflective surface was machined into a curved acrylic globe. However, in that system the outer surface of the acrylic globe functioned only as a transparent, protective cover and a visually non-obstructive support, and had no optical role. There the outer surface was designed to be orthogonal to the incoming rays and therefore did not alter their course. Thus, that system, described in [9], is equivalent to previously described constant-gain surfaces, as in [1], and therefore has a constant elevational gain but not a fixed viewpoint.

II. DERIVATION OF OPTICAL SURFACES

We consider a viewing ray emerging from the nodal point of the camera that is first reflected at the mirror surface and then refracted at the Perspex surface, see Fig. 3. All coordinates will be given in the reference frame of the camera, i.e. the camera’s nodal point defines the origin and its optical axis defines the z -axis. Because of the rotational symmetry we can restrict the derivation to two dimensions. The viewing rays of the overall system should obey the following equation:

$$\mathbf{x}(\lambda, \theta) = \begin{pmatrix} 0 \\ z_v \end{pmatrix} + \lambda \begin{pmatrix} \cos \varepsilon(\theta) \\ \sin \varepsilon(\theta) \end{pmatrix} \quad (5)$$

$$\stackrel{(2)}{=} \mathbf{x}_v + \lambda \mathbf{e}_s(\theta), \quad (6)$$

$$\text{with } \mathbf{e}_s(\theta) = \begin{pmatrix} \sin(\alpha\theta + \beta) \\ -\cos(\alpha\theta + \beta) \end{pmatrix}, \quad \lambda > k(\theta). \quad (7)$$

$\mathbf{x}_v = (0, z_v)^\top$ is the location of the vision system’s single viewpoint where all viewing rays, if extended backwards (see dashed line in Fig. 3), should intersect. As before, the parameters α and β determine the linear mapping between camera angle θ and elevation angle ε , see equation (2), and $\mathbf{e}_s(\theta)$ is the corresponding direction vector. The function $k(\theta)$ defines the distance of the outer surface from the viewpoint (see below).

The *reflective surface* will be parametrised as in equation (3), i.e.

$$\mathbf{x}_m(\theta) = r(\theta) \mathbf{e}(\theta), \quad (8)$$

however with different $r(\theta)$. As derived in appendix, equations (26) – (29), the normal vector of this surface is given by

$$\mathbf{n}_m(\theta) = \frac{-1}{\sqrt{\rho(\theta)^2 + 1}} \begin{pmatrix} -\rho(\theta) \cos \theta + \sin \theta \\ \rho(\theta) \sin \theta + \cos \theta \end{pmatrix}, \quad (9)$$

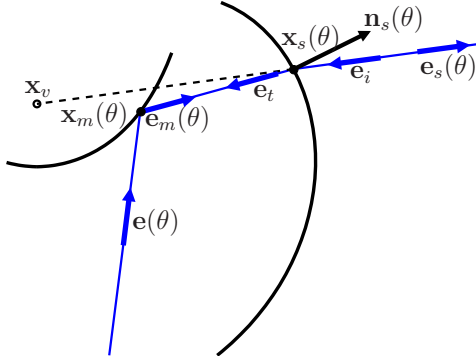


Fig. 3. Illustration of the constraints for the derivation.

where $\rho(\theta) = \frac{r'(\theta)}{r(\theta)}$. Thus, the direction vector of a reflected viewing ray originating from the camera is given by

$$\begin{aligned} \mathbf{e}_m(\theta) &= \mathbf{e}(\theta) - 2(\mathbf{e}(\theta)\mathbf{n}_m(\theta))\mathbf{n}_m(\theta) \\ &= \frac{1}{\rho^2 + 1} \begin{pmatrix} \rho^2 \sin \theta + 2\rho \cos \theta - \sin \theta \\ \rho^2 \cos \theta - 2\rho \sin \theta - \cos \theta \end{pmatrix}. \end{aligned} \quad (10)$$

The *refractive surface* is defined by

$$\mathbf{x}_s(\theta) = \mathbf{x}_v + k(\theta) \mathbf{e}_s, \quad (11)$$

where $k(\theta)$ is the distance of the refractive surface from the viewpoint as a function of the camera angle θ . Similar to (9), the normal vector of the refractive surface (11) is

$$\mathbf{n}_s(\theta) = \frac{-1}{\sqrt{\kappa(\theta)^2 + \alpha^2}} \begin{pmatrix} \kappa(\theta) \cos(\alpha\theta + \beta) - \alpha \sin(\alpha\theta + \beta) \\ \kappa(\theta) \sin(\alpha\theta + \beta) + \alpha \cos(\alpha\theta + \beta) \end{pmatrix}, \quad (12)$$

where we have introduced $\kappa(\theta) = \frac{k'(\theta)}{k(\theta)}$.

We will now derive two constraints ensuring that the imaging system has the desired properties of constant elevational gain and fixed viewpoint.

A. Derivation of 1st constraint

As illustrated in Fig. 3, a viewing ray from the camera, after reflection at the mirror surface $\mathbf{x}_m(\theta)$, has to hit $\mathbf{x}_s(\theta)$, i.e.

$$\mathbf{x}_m(\theta) + \lambda \mathbf{e}_m(\theta) = \mathbf{x}_s(\theta), \quad (13)$$

$$\iff \lambda \mathbf{e}_m(\theta) = \mathbf{x}_s(\theta) - \mathbf{x}_m(\theta). \quad (14)$$

Substituting (8), (10), (11) and dividing the first by the second vector component on both sides of (14), we can solve for $k(\theta)$,

$$k(\theta) = \frac{z_v(r'^2 - r^2) \sin \theta + 2r'r(z_v \cos \theta - r)}{(r'^2 - r^2) \sin[(\alpha+1)\theta + \beta] + 2rr' \cos[(\alpha+1)\theta + \beta]}. \quad (15)$$

Remark: It is interesting to examine when the denominator in (15) will be zero. Solving for r' yields two solutions,

$$r'_1(\theta) = -r(\theta) \cot\left(\frac{\alpha+1}{2}\theta + \frac{\beta}{2}\right), \quad (16)$$

$$r'_2(\theta) = r(\theta) \tan\left(\frac{\alpha+1}{2}\theta + \frac{\beta}{2}\right). \quad (17)$$

The differential equations can be solved in closed form,

$$r_1(\theta) = r_0 \frac{(\sin \frac{\beta}{2})^{\frac{2}{\alpha+1}}}{\sin(\frac{\alpha+1}{2}\theta + \frac{\beta}{2})^{\frac{2}{\alpha+1}}}, \quad (18)$$

$$r_2(\theta) = r_0 \frac{(\cos \frac{\beta}{2})^{\frac{2}{\alpha+1}}}{\cos(\frac{\alpha+1}{2}\theta + \frac{\beta}{2})^{\frac{2}{\alpha+1}}}. \quad (19)$$

The second equation is exactly equation (3) defining a surface of constant elevational gain. Thus, if the mirror surface is a constant elevational gain surface, $k(\theta)$ is not defined and the refractive surface can not be computed, i.e. there exists no refractive surface that can be added in order to achieve a single viewpoint for the whole system.

B. Derivation of 2nd constraint

Next, we calculate the direction \mathbf{e}_t of an incident light ray after refraction at the outer surface. If its initial direction is $\mathbf{e}_i = -\mathbf{e}_s$ (see Fig. 3) then we obtain from Eq. (32) in the appendix with $n_i = 1$, $n_t = n_p$ (the refractive index of Perspex), $\mathbf{n} = -\mathbf{n}_s$ and substituting $\gamma = \sqrt{1 - \frac{1}{n_p^2}(1 - (\mathbf{e}_s \mathbf{n}_s)^2)}$, the normal component of the incident ray after refraction at the air-perspex interface,

$$\begin{aligned} \mathbf{e}_t &= -\left(\gamma \mathbf{n}_s + \frac{1}{n_p}(\mathbf{e}_s - (\mathbf{e}_s \mathbf{n}_s)\mathbf{n}_s)\right), \\ \iff \\ -\mathbf{e}_t - \frac{1}{n_p} \mathbf{e}_s &= \left(\gamma - \frac{1}{n_p} \mathbf{e}_s \mathbf{n}_s\right) \mathbf{n}_s. \end{aligned} \quad (20)$$

As depicted in Fig. 3, $-\mathbf{e}_t$ must be equal to \mathbf{e}_m , the direction vector of the reflected viewing ray. Thus

$$\mathbf{e}_m - \frac{1}{n_p} \mathbf{e}_s = \left(\gamma - \frac{1}{n_p} \mathbf{e}_s \mathbf{n}_s\right) \mathbf{n}_s.$$

Substituting (12), (10), (7) and dividing again the first by the second vector component, we can solve for $\kappa(\theta)$,

$$\kappa(\theta) = \frac{\alpha n_p ((r'^2 - r^2) \sin[(\alpha+1)\theta + \beta] + 2r'r \cos[(\alpha+1)\theta + \beta])}{n_p ((r'^2 - r^2) \cos[(\alpha+1)\theta + \beta] - 2r'r \sin[(\alpha+1)\theta + \beta]) + (r'^2 + r^2)}. \quad (21)$$

C. Differential equation for $r(\theta)$

Since $\kappa(\theta)$ was defined as $\frac{k'(\theta)}{k(\theta)}$ we have

$$\kappa(\theta)k(\theta) = k'(\theta). \quad (22)$$

Substituting (21) and (15) into the left side of (22) and the derivation of (15) w.r.t. θ into the right side of (22) results in a (second order) differential equation that depends on r , r' , r'' and θ . So far, we have not been able to find an analytical solution and thus will use numerical integration to solve for $r(\theta)$, which defines the reflective surface. $k(\theta)$, defining the refractive surface, is then obtained from (15). Solving for r'' we find,

$$\begin{aligned} r'' &= f_r(\theta, r, r'), \\ f_r(\theta, r, r') &= \frac{\alpha n_p g(\theta, r, r')^2 h(\theta, r, r') - m(\theta, r, r') b(\theta, r, r')}{m(\theta, r, r') 2r (r^2 + r'^2) c(\theta, r)}, \end{aligned} \quad (23)$$

where we have used the definitions

$$\begin{aligned}
b(\theta, r, r') &= b_1(\theta, r, r')g(\theta, r, r') - h(\theta, r, r')b_2(\theta, r, r') , \\
b_1(\theta, r, r') &= z_v((3r'^2 - r^2) \cos \theta - 4rr' \sin \theta) - 4rr'^2 , \\
b_2(\theta, r, r') &= ((r'^2 - r^2)(\alpha + 1) + 2r'^2) \cos \xi(\theta) \\
&\quad - 2rr'(\alpha + 2) \sin \xi(\theta) , \\
c(\theta, r) &= (r \sin((\alpha + 1)\theta + \beta) - z_v \sin(\alpha\theta + \beta)) , \\
g(\theta, r, r') &= (r'^2 - r^2) \sin \xi(\theta) + 2rr' \cos \xi(\theta) , \\
h(\theta, r, r') &= z_v((r'^2 - r^2) \sin \theta + 2rr' \cos \theta) - 2r^2r' , \\
m(\theta, r, r') &= n_p((r'^2 - r^2) \cos \xi(\theta) - 2rr' \sin \xi(\theta)) \\
&\quad + r'^2 + r^2 , \\
\xi(\theta) &= (\alpha + 1)\theta + \beta .
\end{aligned} \tag{24}$$

For numerical integration we have to determine starting values θ_0 , $r(\theta_0)$, $r'(\theta_0)$ and fix parameters α , β and z_v . Furthermore we transform (23) into a system of two coupled first order differential equations by introducing $q = r'$,

$$\begin{aligned}
r' &= q , \\
q' &= f_r(\theta, r, q) ,
\end{aligned} \tag{25}$$

where $f_r(\theta, r, q)$ is defined in (23).

III. PROTOTYPE OF IMAGING SYSTEM

For the first realisation of an omnidirectional imaging system with constant elevational gain and single viewpoint the following parameter values were used: For the mapping between camera angle θ and elevation angle ε , equation (2) we chose $\alpha = 5$ (elevational gain) and $\beta = 10 \frac{\pi}{180}$ rad. The z -position of the viewpoint was set to $z_v = 30$ mm. The initial values for numerical integration were $\theta_0 = 5 \frac{\pi}{180}$ rad, $r_0 = 27.5$ mm, $q_0 = r'_0 = 9.6$ mm/rad. Starting values for θ_0 close to zero proved to be problematic for numerical integration. However, this does not pose a serious problem as it is likely to be in the 'blind zone' of the system where the camera sees its own reflection. For the refractive index of acrylic glass we used $n_p = 1.5$.

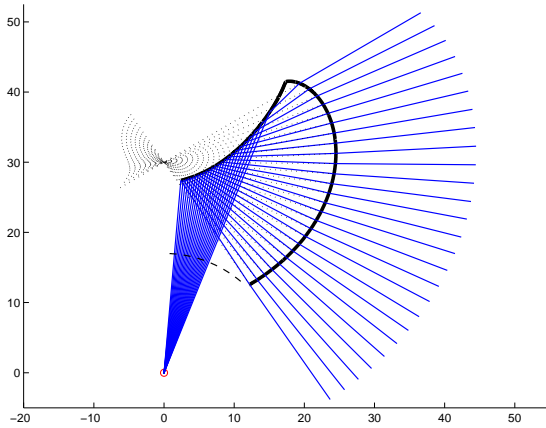


Fig. 4. Raytracing (blue continuous lines) using the calculated reflective and refractive surfaces (thick black curves). The dotted lines show that all rays appear to emerge from a fixed viewpoint at $(0, z_v)$. The dashed curve depicts the concave shape of the perspex surface facing the camera. This surface is spherical, to ensure that it does not refract rays entering the camera.

Fig. 4 shows the profiles of the optical surface that were plotted using the results $r(\theta)$ and $r'(\theta) = q(\theta)$ of the numerical integration of (25) for the specified parameter values. The shape of the reflective surface is given by (8), the shape of the refractive surface is calculated from (11) with $k(\theta)$ defined in (15). Using simple raytracing we verified that the viewing rays emerging from the outer refractive surface have the desired constant elevation gain. Extending these viewing rays backwards, they intersect in a single point (see dotted lines) proving the single viewpoint property of the system.

So far we have implicitly assumed that the rays from the nodal point start inside the acrylic body. As indicated by the dashed curve in Fig. 4, the course of the rays would be unaffected² if we used a concave spherical shape at the camera facing surface (with the nodal point of the camera in the centre of the sphere). However, for simplifying the manufacture of the acrylic body, we decided to use a planar surface. As we will show by raytracing, this affects the system's characteristics only marginally.

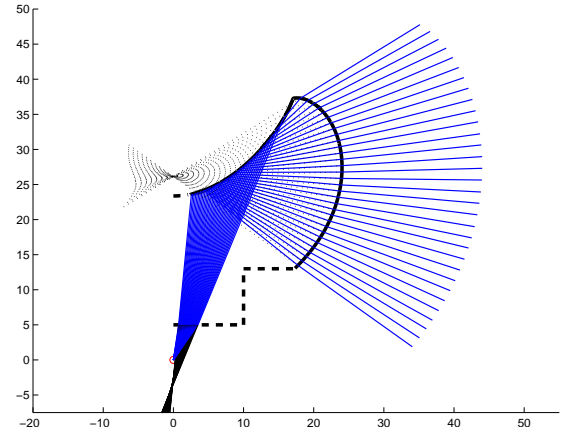


Fig. 5. Shape of the acrylic body as manufactured for our prototype, Fig. 6. The cylindrical shaft and the planar surface facing the camera are depicted by dashed lines.

For the machining of the acrylic body, we extended the profile of the reflective surface in the range $|\theta| < \theta_0$ using an arc tangent to the surface at $\pm\theta_0$. In addition, a short cylindrical shaft (length 9 mm, diameter 20 mm) was introduced for mounting the acrylic body onto the CNC lathe to facilitate machining and subsequent attachment to the body of the camera lens. The resulting shape of the acrylic body is shown in Fig. 5. As can be seen from the raytracing for this profile (Fig. 5), the single-viewpoint property still holds in quite good approximation. However, due to the refraction at the planar surface, the effective FOV of the camera is reduced and the effective nodal point is shifted in z by approx. -4 mm, as is the viewpoint. As a result the camera lens has to be placed 4 mm closer to the reflective surface, compared to when a spherical concavity is used. In addition, although the elevational gain is still constant in very good approximation,

²Of course, depth of focus would change because only principal rays would hit the surface perpendicularly.

it is reduced from $\alpha = 5$ to $\alpha_{\text{eff}} \approx 3.2$. The elevation range of our prototype is approximately $\varepsilon \in [-35^\circ, 32^\circ]$. Thus, the camera lens has to have a vertical FOV of about 70° (since $\alpha_{\text{eff}} \times 70^\circ / 2 + \beta - 90^\circ = 32^\circ$).

A. Manufacture

After CNC-machining, the acrylic body was hand-polished on a lathe and the reflective surface was produced by a vapour-deposited layer of aluminium. For mounting onto the camera lens a cylindrical element was machined from plastic. A plastic cap was fitted over the concave opening at the top to protect the thin aluminium layer and prevent unwanted light entering the camera from above, see Fig. 6. Images captured with the omnidirectional imaging system are shown in Fig. 7.



Fig. 6. Picture of the first prototype of an omnidirectional imaging system with constant elevational gain and single viewpoint. Diameter of the transparent globe is 48 mm.

B. Calibration Results

In order to examine the imaging properties of our prototype, we calibrated the imaging system using the “OCamCalib” Matlab toolbox [10]. Since the camera model of this toolbox assumes a single viewpoint, a large reprojection error for points of the calibration pattern, in particular for images where the calibration board was held close to the camera, would be a good indicator that the single viewpoint property is violated. However, mean reprojection error (for 12 images) was low, approximately 0.47 pixels. The image with the highest average reprojection error (0.57 pixels) is shown in Fig. 8. The size of the calibration pattern (a 9×7 checker board printed on A4 paper that was glued onto a Perspex plate) was 216 mm \times 168 mm.

As illustrated in Fig. 9, the mapping of elevation angle ε to radial distance from image centre ϱ is almost linear. Note that a slight deviation from a perfect linear mapping is to be expected for larger ϱ values since the perspective projection of the camera lens maps ϱ to camera angle θ according to



Fig. 7. Two examples of captured images (480×480 pixels).

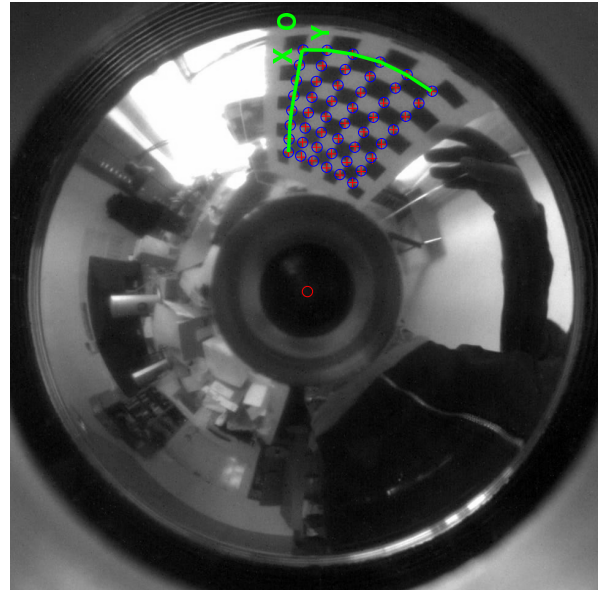


Fig. 8. Illustration of the good fit of the single viewpoint camera model of the OCamCalib calibration toolbox [10] for our prototype. Distance of the calibration board to the imaging system was about 15 cm. Small red crosses mark the automatically detected corners of the calibration pattern. Blue circles show the reprojected points computed from the known geometry and the estimated calibration parameters. The small red circle depicts the image centre as estimated by the calibration toolbox.

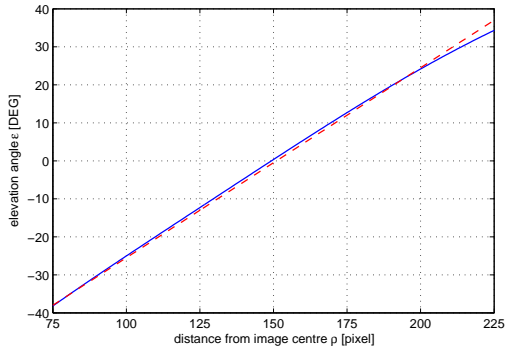


Fig. 9. Result of calibration, showing the measured mapping between elevation angle ε and radial distance ρ from the image centre for ρ varying from 75 to 225 pixels. The dashed red line shows, for comparison a perfectly linear mapping represented by $\varepsilon = -38^\circ + 0.5^\circ/\text{pixel}(\rho - 75 \text{ pixel})$.

$\theta = \arctan(\rho/f)$, where f is the focal length of the lens in pixels. Thus, using Eq. (2) and ignoring distortions introduced by real lenses, the mapping with respect to elevation angle is $\varepsilon = \alpha \arctan(\rho/f) + \beta$.

We conclude from the results of the calibration procedure that our prototype is indeed, at least in good approximation, a single viewpoint imaging system with constant elevational gain.

IV. SENSITIVITY TO SHIFTS ALONG z -AXIS

For the derivation of the surfaces and the results presented in the previous section we assumed that the nodal point of the camera is located at the origin of the coordinate system. In the following we investigate the effect of a shift of the nodal point along the z -axis. This is of particular interest since the exact position of the nodal point of the camera lens along the optical axis is often hard to determine.

Fig. 10 shows raytracing results using the same shape of the optical surfaces as in Fig. 4 but with the nodal point shifted by $\Delta z = \pm 15 \text{ mm}$. Despite these quite large shifts there are only very small deviations visible from a fixed viewpoint system. However, the position of the (approximate) viewpoint changes, as does the elevational gain α of the whole system. As depicted in Fig. 11, the over-all elevational gain increases for $\Delta z < 0$ and decreases for $\Delta z > 0$. While elevational gain

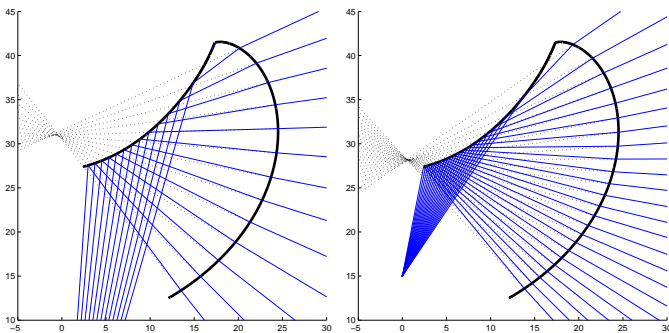


Fig. 10. Raytracing results for a shift of the nodal point along the optical axis by an amount $\Delta z = -15 \text{ mm}$ (left) or $\Delta z = +15 \text{ mm}$ (right).

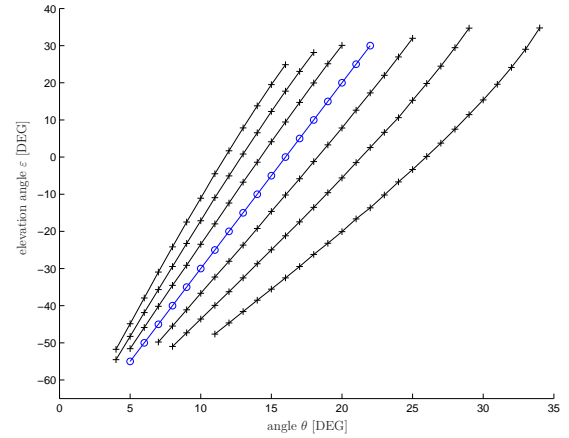


Fig. 11. Elevation angle ε versus camera angle θ for (from left to right) $\Delta z = -15 \text{ mm}, -10 \text{ mm}, -5 \text{ mm}, 0 \text{ mm}, +5 \text{ mm}, +10 \text{ mm}, +15 \text{ mm}$. ε and θ are as defined in Fig. 1. For $\Delta z = 0 \text{ mm}$, we have the linear mapping $\varepsilon = \alpha\theta + \beta$.

is nevertheless almost constant for small shifts (see curves for $\Delta z = \pm 5 \text{ mm}$) significant deviations from a linear relationship between angle θ and elevation angle ε become visible for $|\Delta z| \geq 10 \text{ mm}$.

V. CONCLUSION

The use of an additional refractive surface gives the opportunity to incorporate additional desirable properties in an omnidirectional imaging system. In this paper we have used this approach to construct a single-viewpoint system with constant elevational gain. In addition, the machining of the reflective surface into a globe of acrylic glass enables the construction of compact, rugged omnidirectional imaging systems without any obstructing parts. Future work will include analysis of image blur and optimal focus settings.

ACKNOWLEDGEMENTS

We thank the machine shops at the Institute of Robotics and Mechatronics (DLR) and Bielefeld University for machining the parts of the omnidirectional imaging system.

This research was partly supported by the Deutsche Forschungsgemeinschaft (DFG) and by grants from the US Army Research Office MURI ARMY-W911NF041076, Technical Monitor Dr Tom Doligalski, ARC Centre of Excellence Grant CE0561903, and a Queensland Smart State Premier's Fellowship to MVS.

REFERENCES

- [1] J. Chahl and M. Srinivasan, "Reflective surfaces for panoramic imaging," *Applied Optics*, vol. 36, pp. 8275–8285, 1997.
- [2] S. Baker and S. K. Nayar, "A theory of single-viewpoint catadioptric image formation," *International Journal of Computer Vision*, vol. 35, pp. 175–196, 1999.
- [3] R. Benosman and S. B. Kang, *Panoramic Vision: Sensors, Theory and Applications*, 1st ed. Springer, Berlin, 2001.
- [4] W. Stürzl, H.-J. Dahmen, and H. Mallot, "The quality of catadioptric imaging – application to omnidirectional stereo," in *ECCV, 2004*, pp. 614–627.
- [5] R. Swaminathan, M. Grossberg, and S. Nayar, "Caustics of catadioptric cameras," in *ICCV, 2001*, pp. 2–9.

- [6] S. Baker and S. Nayar, "Single viewpoint catadioptric cameras," in *Panoramic Vision*, R. Benosman and S. Kang, Eds., 2001, pp. 39–70.
- [7] R. Hicks, M. Millstone, and K. Daniilidiis, "Realizing any central projection with a mirror pair," *Applied Optics*, vol. 45, pp. 7205–7210, 2006.
- [8] H. Nagahara, K. Yoshida, and M. Yachida, "An omnidirectional vision sensor with single view and constant resolution," *ICCV*, pp. 1–8, 2007.
- [9] W. Stürzl, D. Soccol, J. Zeil, N. Boeddeker, and M. Srinivasan, "A rugged, obstruction-free, mirror-lens combination for panoramic imaging," *Applied Optics*, vol. 47, pp. 6070–6078, 2008.
- [10] D. Scaramuzza, A. Martinelli, and R. Siegwart, "A toolbox for easily calibrating omnidirectional cameras," in *IROS*, 2006, pp. 5695–5701.

APPENDIX I: SURFACE NORMAL VECTOR

For a surface in 3D that is parameterised by two parameters, $\mathbf{x}_s(s, t)$, the normal vector is given by

$$\mathbf{n}_s(s, t) = \frac{\frac{\partial}{\partial s} \mathbf{x}_s(s, t) \times \frac{\partial}{\partial t} \mathbf{x}_s(s, t)}{\left\| \frac{\partial}{\partial s} \mathbf{x}_s(s, t) \times \frac{\partial}{\partial t} \mathbf{x}_s(s, t) \right\|}. \quad (26)$$

For surfaces of revolution parameterised in spherical coordinates,

$$\begin{aligned} \mathbf{x}_s(\phi, \theta) &= r(\theta) \mathbf{e}(\phi, \theta), \\ \mathbf{e}(\phi, \theta) &= (\cos \phi \sin \theta, \sin \phi \sin \theta, \cos \theta)^\top \end{aligned} \quad (27)$$

we obtain from (26):

$$\begin{aligned} \mathbf{n}_s(\phi, \theta) &= \frac{\mathbf{x}_n}{\|\mathbf{x}_n\|}, \\ \mathbf{x}_n &= \begin{pmatrix} \cos \phi (r'(\theta) \cos \theta - r(\theta) \sin \theta) \\ \sin \phi (r'(\theta) \cos \theta - r(\theta) \sin \theta) \\ -r'(\theta) \sin \theta - r(\theta) \cos \theta \end{pmatrix}, \quad (28) \\ \|\mathbf{x}_n\| &= \sqrt{r'(\theta)^2 + r(\theta)^2}. \end{aligned}$$

If we consider just the radial direction and the z -direction this simplifies to

$$\begin{aligned} \mathbf{n}_s(\theta) &= \frac{-1}{\sqrt{r'(\theta)^2 + r(\theta)^2}} \begin{pmatrix} -r'(\theta) \cos \theta + r(\theta) \sin \theta \\ r'(\theta) \sin \theta + r(\theta) \cos \theta \end{pmatrix} \\ &= \frac{-1}{\sqrt{\rho(\theta)^2 + 1}} \begin{pmatrix} -\rho(\theta) \cos \theta + \sin \theta \\ \rho(\theta) \sin \theta + \cos \theta \end{pmatrix}, \quad (29) \end{aligned}$$

where we have defined $\rho(\theta) = \frac{r'(\theta)}{r(\theta)}$ (assuming $r(\theta) \neq 0$).

APPENDIX II: REFRACTION

In order to calculate the direction vector \mathbf{e}_t of the transmitted ray, it is split into components parallel and orthogonal to the surface of refraction, see Fig. 12,

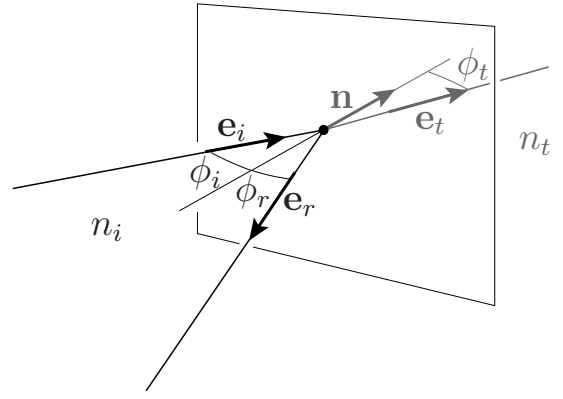


Fig. 12. Hitting a surface of different refraction index, a light ray with direction vector \mathbf{e}_i is partly reflected into direction \mathbf{e}_r and partly transmitted into direction \mathbf{e}_t .

$$\mathbf{e}_t = \mathbf{e}_{t\parallel} + \mathbf{e}_{t\perp}. \quad (30)$$

Snell's law,

$$n_t \sin \phi_t = n_i \sin \phi_i, \quad (31)$$

is equal to

$$\begin{aligned} n_t \mathbf{e}_{t\parallel} &= n_i \mathbf{e}_{i\parallel} \\ \Leftrightarrow \mathbf{e}_{t\parallel} &= \frac{n_i}{n_t} (\mathbf{e}_i - (\mathbf{e}_i \mathbf{n}) \mathbf{n}). \end{aligned}$$

The component orthogonal to the surface is

$$\mathbf{e}_{t\perp} = \gamma \mathbf{n},$$

where γ can be calculated from the constraint

$$\begin{aligned} \mathbf{e}_t^2 &= \mathbf{e}_{t\parallel}^2 + \gamma^2 = 1 \\ \Leftrightarrow \gamma^2 &= 1 - \frac{n_i^2}{n_t^2} (\mathbf{e}_i - (\mathbf{e}_i \mathbf{n}) \mathbf{n})^2 \\ &= 1 - \frac{n_i^2}{n_t^2} (1 - (\mathbf{e}_i \mathbf{n})^2). \end{aligned}$$

Thus, the direction of the refracted ray is (for $\mathbf{e}_i \mathbf{n} > 0$)

$$\mathbf{e}_t = \sqrt{1 - \left(\frac{n_i}{n_t}\right)^2 (1 - (\mathbf{e}_i \mathbf{n})^2)} \mathbf{n} + \frac{n_i}{n_t} (\mathbf{e}_i - (\mathbf{e}_i \mathbf{n}) \mathbf{n}). \quad (32)$$